Supplementary Material

Investigating Surface Effects of GaN Nanowires Using Confocal Microscopy at Below-Band Gap Excitation

Lauren R. Richey-Simonsen[†], Nicholas J. Borys[†], Tevye R. Kuykendall[‡], P. James Schuck[‡], Shaul Aloni[‡], and Jordan M. Gerton[†]

[†] Department of Physics & Astronomy, University of Utah, 115 S. 1400 E., Salt Lake City, UT, 84112, USA
[‡] Molecular Foundry, Lawrence Berkeley National Laboratory, Berkeley, CA, 94720, USA

Wurtzite Crystalline Structure

During epitaxial growth, gallium nitride (GaN) can be grown into both a face-centered cubic crystalline structure (zinc-blende) or a hexagonal crystalline structure (wurtzite)[1]. In our samples, nanowires (NWs) were grown into a wurtzite crystalline structure that exhibits hexagonal geometry whose planes and directions are described by four indices (a1, a2, a3, c). Different surfaces exhibit polar or non-polar properties depending upon their relative orientation to the lattice dipole moment. Polar planes are perpendicular to the polarization vector, non-polar planes are parallel to the polarization vector, and semi-polar planes are at an angle to the polarization vector[2].

For this work, wires were grown along the *a*-axis in the [11-20] direction perpendicular to the non-polar *a*-plane (see Fig. S1a). TEM analysis showed that the resulting triangular cross section of the wires exhibited three surfaces: (0001) polar surface (or commonly known as the *c*-plane), (-1101) semi-polar surface, and (1-101) semi-polar surface[3]. It is important to note that the two semi-polar planes are the same except for the signs on the a1 and a2 directions (see Fig. S1).

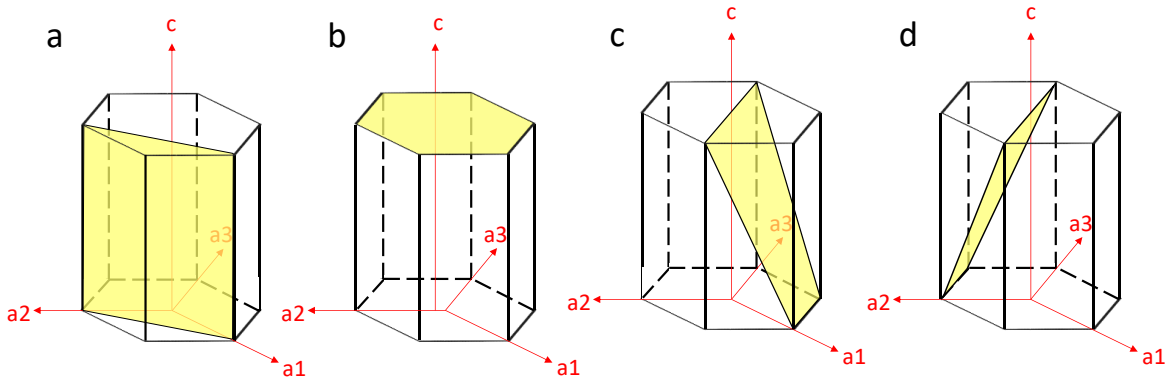

Fig. S1: Wurtzite crystal structure with highlighted planes. **(a)** (11-20) non-polar plane, **(b)** (0001) polar plane **(c)** (1-101) semi-polar plane, and **(d)** (-1101) semi-polar plane.

SCOM-Intensity Plots:

The position of pixels in SCOM-Intensity plots (and their corresponding positions on integrated intensity and SCOM images) provides information about the interaction of the diffraction-limited excitation beam (~350 nm spot size) with the NW, halo, and glass substrate pixels. SCOM-Intensity plots (S-I plots) of image patterns exhibiting radial asymmetry (RA) have two branches

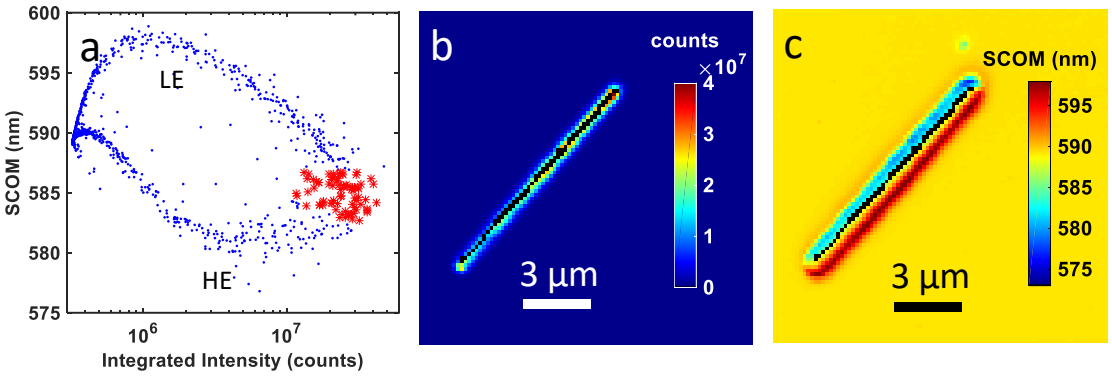

Fig. S2: (a) S-I plot of a two-phase patterned NW (same as Fig. 3) with red asterisks corresponding to the high intensity meeting point of the red and blue branches. **(b)** Integrated intensity image of the NW with white pixels indicating the selected pixels (middle/apical ridge) shown in panel a. **(c)** SCOM image of the NW with black pixels indicating the selected pixels shown in panel a.

(corresponding to the low energy (LE) and high energy (HE) sides of the NW) that meet at high and low integrated intensity. The meeting point at high signal intensity corresponds to the middle of the NW, or apical ridge, as the diffraction-limited laser excites both surfaces (see Fig. S2). The meeting point at low signal intensity contains a large number of pixels at a similar intensity and SCOM value (~590 nm), corresponding to surrounding pixels on the glass substrate (background).

When the excitation laser is positioned just off the apical ridge towards the HE side (bottom branch in Fig. S2a), the pixel intensity decreases as the laser beam begins to slide off the NW. This leads to two competing effects: a reddening of the emission caused by a decrease in the effective laser power illuminating the NW, and a bluing of the emission caused by less illumination of the LE side of the NW. This competition leads to a rather gentle slope and flattening of the HE branch moving from high to low pixel intensities. As the laser beam moves further away from the NW apex on the HE side, the pixel intensities decrease further and the reddening effect begins to dominate, thereby reversing the slope of the S-I curve below $\sim 5\times10^6$ counts along the HE branch. As the laser beam moves outward from the NW apex on the LE side of the NW (upper branch in Fig. S2a), the reddening caused by a decrease in effective laser power supplements the reddening caused by less illumination of the HE side. Thus, the slope of the LE branch of the S-I curve moving from high to low pixel intensities is steeper compared to the HE branch.

Figure S3 demonstrates the correlation between low intensity pixels and the halo which surrounds the NW in SCOM images. In Fig. S3a, which corresponds to a NW image exhibiting radial uniformity (RU), pixel intensities below $\sim 7 \times 10^5$ counts correspond to spatial positions of the laser beam along the periphery of the NW (see Fig. S3b and c). In Fig. S3d, which corresponds to a NW image exhibiting radial asymmetry (RA), pixels intensities between $\sim 7 \times 10^5$ and $\sim 5 \times 10^6$ counts map to points on the NW periphery where the laser beam illuminates both the NW and the

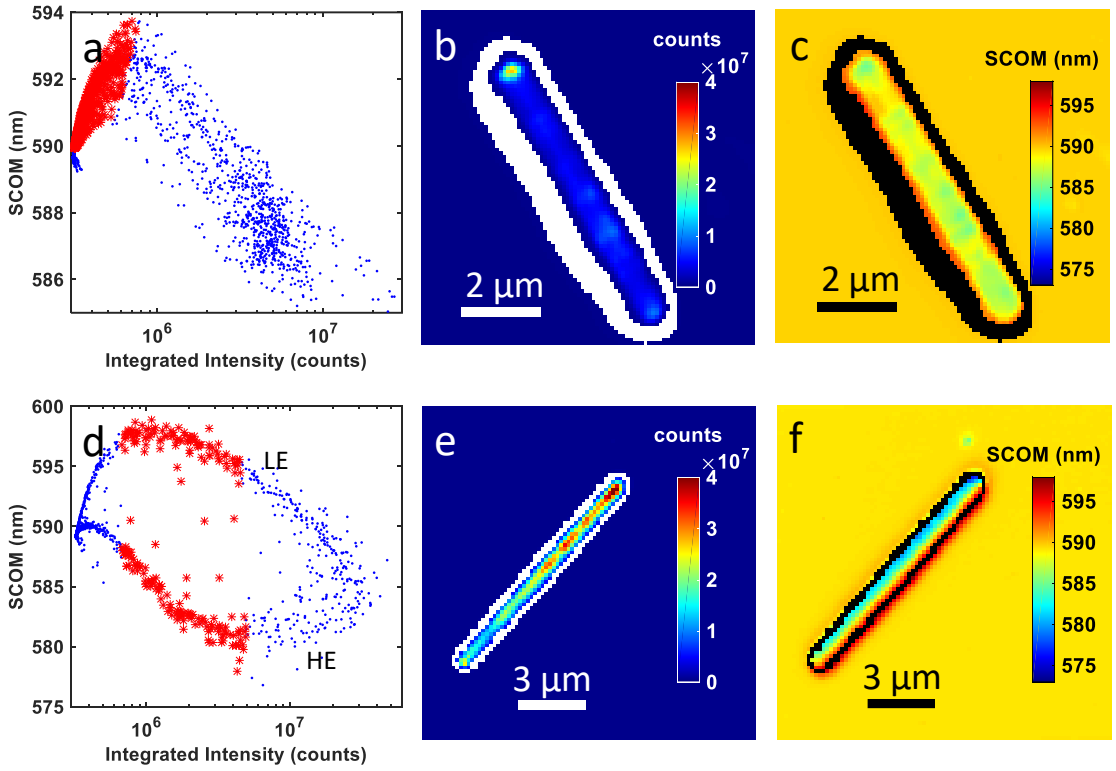

Fig. S3: (a) S-I plot of a NW exhibiting an RU image pattern (corresponding to Fig. 2) with selected pixels as red asterisks. **(b)** Intensity image showing selected pixels from panel a in white along the periphery of the NW. **(c)** SCOM image showing selected pixels from panel a in black. **(d)** S-I plot of a NW exhibiting an RA image pattern (corresponding to Fig. 3) with selected pixels as red asterisks. **(e)** Intensity image showing selected pixels from panel d in white along the periphery of the NW. **(f)** SCOM image showing selected pixels from panel d in black.

halo region simultaneously (see Figs. S3e and f). As the laser beam moves further away from the central axis of the NW, the pixel intensities become smaller, causing the HE branch of the S-I plot to redden. However, the LE branch becomes more blue, which may be caused by the laser beam overlap with the bluer glass substrate. Below $\sim 5 \times 10^5$ counts, the laser beam predominately illuminates the glass substrate, which has a distinct spectral signature compared to the halo (see below). Thus, the LE and HE branches eventually converge at the lowest pixel intensities with an HE branch inflection point at $\sim 5 \times 10^5$ counts.

The S-I plots show that the (0001) and the (1-101)/(-1101) surfaces do have distinct spectral characteristics. The slow changes in the S-I plots for RA image patterns suggests that the PL

should be modeled by the convolution of the response of the two surfaces (see Gaussian fits below). Furthermore, the S-I plots propose caution in measuring the fluorescence of entire NW forests, or even isolated nanoscopic systems as a whole, as spectral properties can vary dramatically at different spatial locations.

Nanowire Halos:

The halo region is a red-shifted area in background-subtracted SCOM images (see Fig. S4a) which roughly corresponds to the pixels selected in Fig. S3a. Spectra selected from the NW, edge of the NW, halo region, and glass substrate are shown in Fig. S4b and c. As the diffraction-limited excitation laser moves from the NW body to the edge, the intensity decreases and redshifts. The resulting spectra from the halo region is very weak (Fig. S4c) but clearly shows signal that is

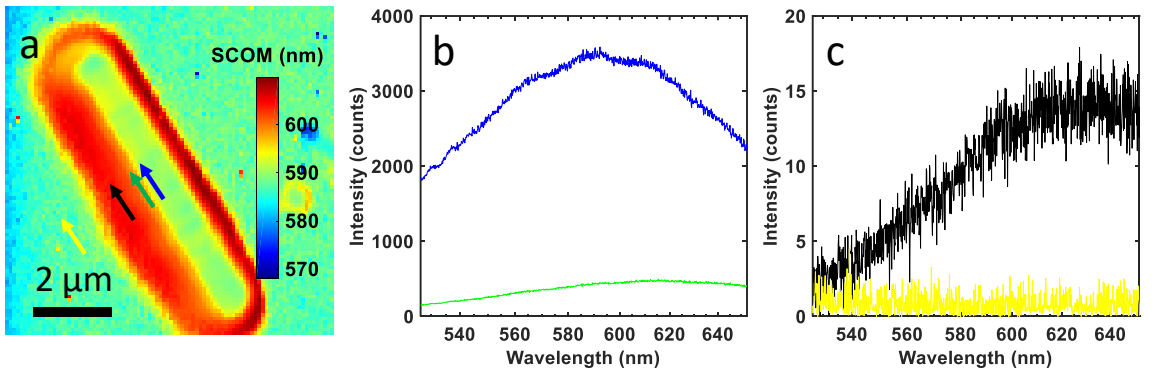

Fig. S4: (a) SCOM interpolated image of a NW (corresponding to Fig. 2) using pixels that were background subtracted, showing a red-shifted halo region surrounding the NW. **(b)** Higher intensity spectra on the NW and on the edge of the NW indicated by corresponding colored arrows in panel a. **(c)** Low intensity spectra in the halo region and from the background-subtracted glass substrate as indicated by corresponding colored arrows in panel a.

distinct from both the NW and the glass substrate. The absolute value was taken after background subtraction to eliminate negative count values, which created large SCOM fluctuations in the glass substrate areas of the SCOM images (see yellow spectra in Fig. S4c).

A background subtracted image for a NW exhibiting an RA pattern is shown in Fig. S5 emphasizing the halo, but diminishing the starkness of the RA effect. For NWs with RA patterns, the spectra along the periphery of one side of the NW is relatively blue shifted while the other side is relatively red shifted. This suggests that the diffraction-limited excitation beam partially overlaps the NW surface, halo, and glass substrate to produce a combined effect. Note that the red-sided halo spectra in Fig. S5b roughly corresponds to the halo spectra in Fig. S4c, indicating that these wires produce a similar halo response due to a shared (1-101)/(-1101) surface.

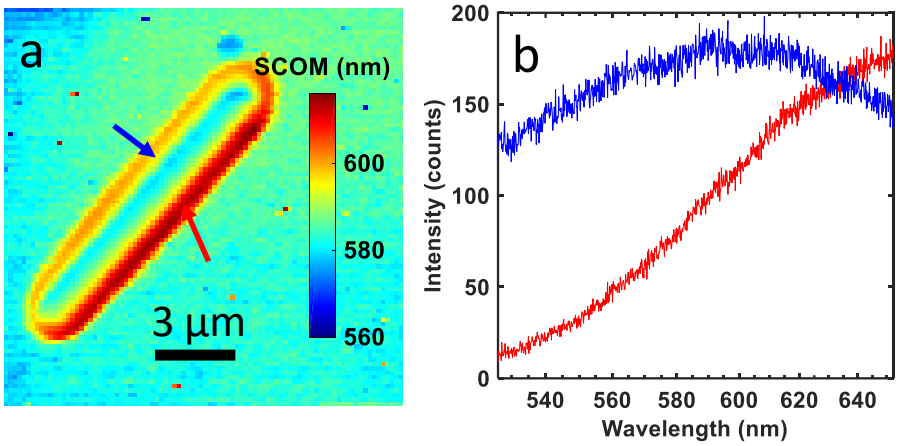

Fig. S5: (a) SCOM interpolated image of the NW (corresponding to Fig. 3) using pixels that were background subtracted. **(b)** Spectra from the left ((0001) surface) and right ((1-101)/(-1101) surface) sides of the halo as indicated by the corresponding colored arrows shown in panel a.

Linear Power Dependence

Power dependent measurements confirm that the surface-associated mid-gap states were excited directly by the 488-nm excitation rather than two-photon absorption into the conduction band followed by relaxation into the mid-gap states. Hyper-spectral images of NWs at various excitation intensities were acquired using neutral density filters and the overall average pixel intensity was calculated. When the average pixel intensity is plotted vs. laser power on a log-log scale, the slope of the resulting curve indicates the photon order[4, 5], which in this case is consistent with a linear scattering process (see Fig. S6). The sharp transition between a flat and linear

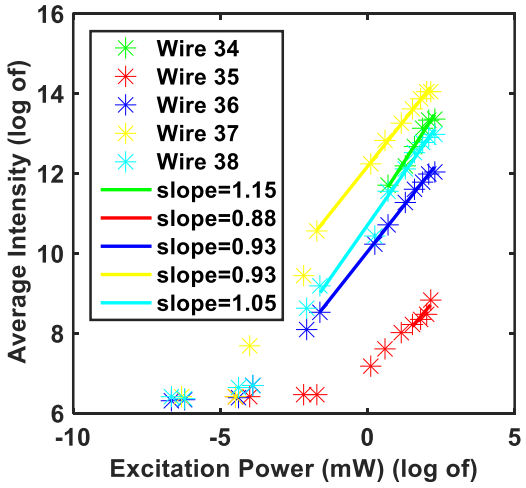

Fig. S6: Log-log plots of the average pixel intensity as a function of excitation power for several NWs. The data is consistent with a photon order of one, suggesting a linear scattering process; i.e., direct excitation into mid-gap states.

response reflects when the collected signal exceeds the background, rather than indicating a true threshold process (e.g., lasing).

Etalon Fringes:

Etalon fringes were observed at the ends of the NWs due to multiple reflections of emitted photons within the NW cavity[4]. While some NWs exhibited fringes in the spectra at the ends of the NWs, others did not. This is most likely due to the absence of cleanly-cleaved NW ends needed to create the high reflective surfaces required for interference fringes.

NW end spectra corresponding to different lengths of nanowires are shown in Fig. S7 with red lines indicating maxima of selected fringes. The free spectral range (FSR) of an etalon corresponds to the wavelength spacing between successive fringes and is given by:

$$\mathrm{FSR} = \frac{\lambda_o^2}{2nl\cos\theta},$$

where FSR is in nm, λ_o is the peak wavelength of the nearest fringe, n is the index of refraction of the material (roughly 2.5 for GaN), l is the length of the NW, and θ is the angle of light entering the etalon/NW[6]. For $\theta = 0$, light enters along the longitudinal axis of the NW and the formula above for FSR can be used to estimate the length of the NW. The length of the NW can also be

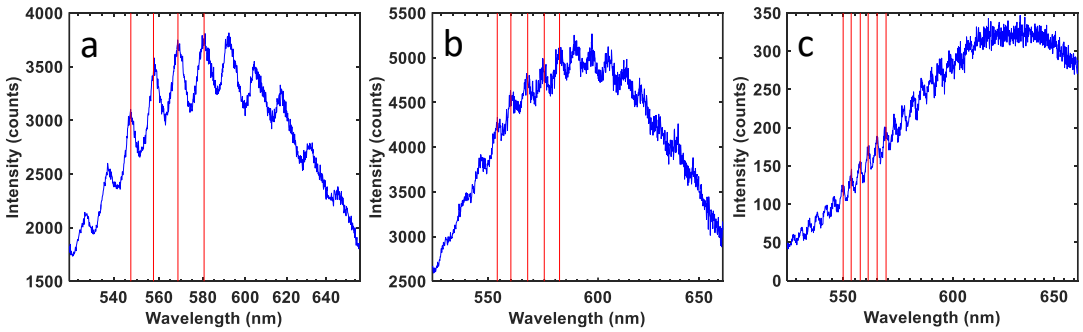

Fig. S7: Spectra from the ends of three different NWs with **(a)** shorter, **(b)** medium, and **(c)** longer lengths. Panel a and b correspond to the NWs in Figs. 1 and 2 respectively. Red vertical lines mark the maximum points on selected fringes.

estimated directly from intensity images taking into account the diffraction-limited size of the laser focus. Comparisons between these two ways of estimating the NW length are summarized in Fig. S7.

Dual Gaussian Fitting:

Individual spectra along the NW were fit to a dual Gaussian model:

$$A_1 e^{-(x-\mu_1)^2/(2\sigma_1^2)} + A_2 e^{-(x-\mu_2)^2/(2\sigma_2^2)} + B,$$

where A is the amplitude, μ is the Gaussian center, σ^2 is the variance, and B is the background. The FWHM of the Gaussian was calculated from the variance: $FWHM = 2\sqrt{2\ln(2)}\,\sigma$ with the background set to a relatively small range of fitting parameters. In the fits, the centers and variance of the Gaussian were fixed parameters based on literature values and a χ^2 analysis, while the amplitudes A_1 and A_2 were allowed to vary. The Gaussian centers used were 2.26 +/- 0.1 eV and 1.99 +/- 0.1 eV with FWHM for both Gaussians at 0.365 eV.

RA NWs varied in fit amplitude from one side of the longitudinal axis to the other (see Fig. 5 in main paper), while Δ_{norm} (see main paper) maps of one-phase patterned NWs varied very little from one side of the longitudinal axis to the other (see Fig. S8).

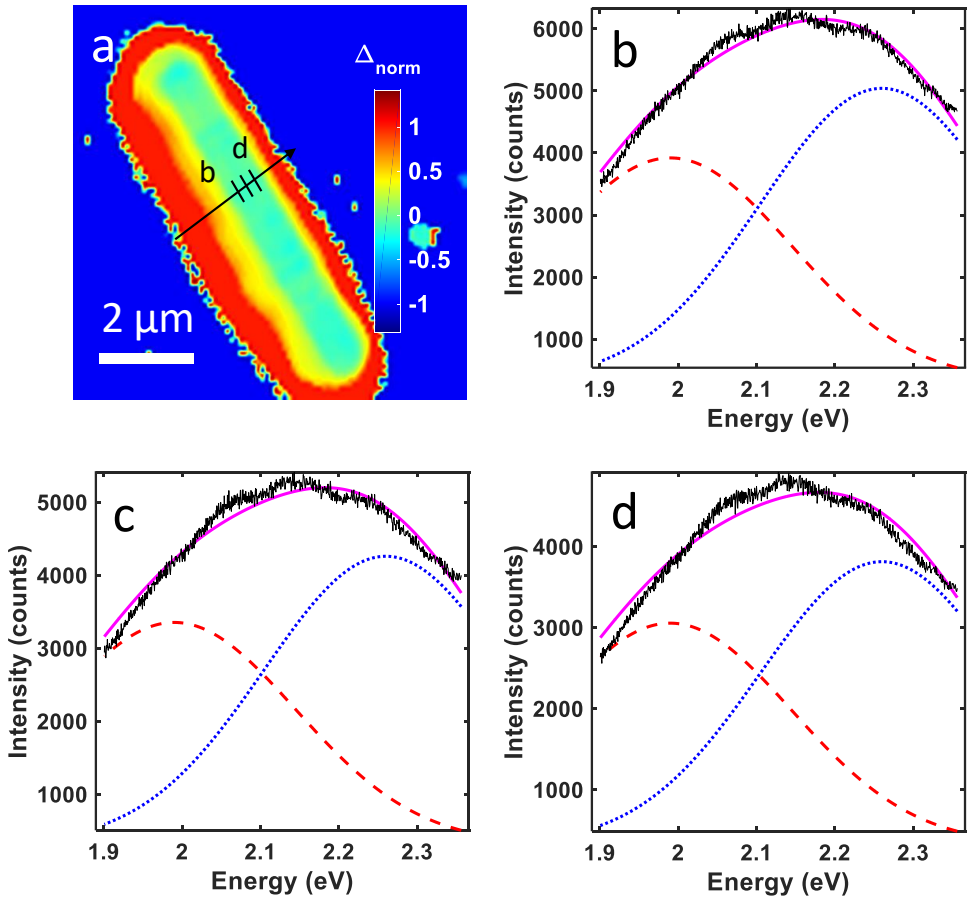

Fig. S8: Gaussian amplitude map of the NW shown in Fig. 2. **(a)** Δ_{norm} image as defined by Eqn. 2. **(b,c,d)** Spectra (black line) from different spatial locations were fit to the superposition of two Gaussian functions (purple fit line), one centered at 2.26 eV with FWHM 0.365 eV (blue dotted line) and another centered at 1.99 eV with FWHM 0.365 eV (red dashed line). The spectra in (b)-(d) were extracted from the positions indicated by the line profile and corresponding cross hatches in panel a.

Citations:

1. H. Morkoç: Nitride Semiconductor Devices: Fundamentals and Applications (Wiley-VCH Verlag GmbH & Co. KGaA, Weinheim, Germany, 2013), pp. 2.

2. A. Konar, A. Verma, T. Fang, P. Zhao, R. Jana and D. Jena: Charge transport in non-polar and semi-polar III-V nitride heterostructures. *Semicond. Sci. Technol.* **27**(2), 024018 (2012).

3. T.R. Kuykendall, M.V.P. Altoe, D.F. Ogletree and S. Aloni: Catalyst-Directed Crystallographic Orientation Control of GaN Nanowire Growth. *Nano Lett.* **14**, 6767 (2014).

4. A.M. Schwartzberg, S. Aloni, T. Kuykendall, P.J. Schuck and J.J. Urban: Optical cavity characterization in nanowires via self-generated broad-band emission. *Opt. Express* **19**(9), 8903 (2011).

5. Lakowicz: Principles of Fluorescence Spectroscopy, 2nd ed. (Kluwer Academic/Plenum Publishers, New York, NY, 1999), pp. 58.

6. G.R. Fowles: Introduction to Modern Optics, 2nd ed. (Holt, Rinehart, and Winston, New York, NY, 1975), pp. 94.